Marquette University
e-Publications@Marquette

Biological Sciences Faculty Research and Publications

Biological Sciences, Department of

5-1-1995

Quantitative Analysis of Electrotonic Structure and Membrane Properties of NMDA-Activated Lamprey Spinal Neurons

C. R. Murphey
University of Texas Medical Branch

L. E. Moore
Karolinska Institute

James T. Buchanan
Marquette University, james.buchanan@marquette.edu

Quantitative Analysis of Electrotonic Structure and Membrane Properties of NMDA-Activated Lamprey Spinal Neurons

C. R. Murphey
Department of Physiology and Biophysics, University of Texas Medical Branch, Galveston, TX 77555-0641 USA

L. E. Moore
Department of Physiology and Biophysics, University of Texas Medical Branch, Galveston, TX 77555-0641 USA and
Department of Neurobiology, CNRS, University of Rennes I, 35042 Rennes Cedex France

J. T. Buchanan
Department of Biology, Marquette University, Milwaukee, WI 53233 USA

Parameter optimization methods were used to quantitatively analyze frequency-domain-voltage-clamp data of NMDA-activated lamprey spinal neurons simultaneously over a wide range of membrane potentials. A neuronal cable model was used to explicitly take into account receptors located on the dendritic trees. The driving point membrane admittance was measured from the cell soma in response to a Fourier synthesized point voltage clamp stimulus. The data were fitted to an equivalent cable model consisting of a single lumped soma compartment coupled resistively to a series of equal dendritic compartments. The model contains voltage-dependent NMDA sensitive (I_{NMDA}), slow potassium (I_K), and leakage (I_L) currents. Both the passive cable properties and the voltage dependence of ion channel kinetics were estimated, including the electrotonic structure of the cell, the steady-state gating characteristics, and the time constants for particular voltage- and time-dependent ionic conductances. An alternate kinetic formulation was developed that consisted of steady-state values for the gating parameters and their time constants at half-activation values as well as slopes of these parameters at half-activation. This procedure allowed independent restrictions on the magnitude and slope of both the steady-state gating variable and its associated time constant. Quantitative estimates of the voltage-dependent membrane ion conductances and their kinetic parameters were used to solve the nonlinear equations describing dynamic responses. The model accurately predicts current clamp responses and is consistent with experimentally measured TTX-

resistant NMDA-induced patterned activity. In summary, an analysis method is developed that provides a pragmatic approach to quantitatively describe a nonlinear neuronal system.

1 Introduction

An understanding of the locomotion neural network is critically dependent on the biophysical properties of individual neurons. Although quantitative methods have been used on a variety of different neurons, it continues to be difficult to obtain sufficient data to completely characterize intact neurons with their complex dendritic trees (Jonas et al. 1993; Rapp et al. 1994). Previous studies using frequency domain techniques have demonstrated a way to explicitly take into account the dendritic cable properties (Moore and Buchanan 1993). This approach provides a substantial improvement over conventional techniques and provides a partial solution to the space clamp problems of highly branched neurons. This paper presents a detailed quantitative kinetic analysis of voltage-dependent conductances using the above combination voltage-clamp-frequency-domain technique. The analysis provides quantitatively determined parameters from frequency domain data for a previously proposed nonlinear model of N-methyl-D-aspartate (NMDA)-activated conductances (Moore and Buchanan 1993).

The goal of this analysis is to obtain a minimal nonlinear kinetic model of individual neurons having a dendritic cable. Fundamentally, our approach is analogous to that used by Hodgkin and Huxley (HH) who measured linear kinetic parameters at different voltage clamp potentials to obtain the voltage dependence of the rate constants (Hodgkin and Huxley 1952). In the HH analysis the voltage dependence of the rate constants was empirically described by combinations of exponential functions that provided the principal nonlinear behavior of the basic membrane equations. The quantitative analysis of neurons is more difficult since the ionic conductances are distributed over cable structures. Nevertheless, a comparable formalism can be used, namely the determination of linear kinetic parameters at fixed membrane potentials using small-signal linear analysis methods rather than relaxation responses to step potential functions. We obtain the whole cell driving point characteristic by measuring the soma membrane current in response to a small-signal soma voltage clamp stimulus composed of a sum of sinusoids superimposed on a steady clamp potential. The response and stimulus are transformed to the frequency domain by a fast Fourier method and at each given frequency the ratio of the measured current to the stimulus voltage gives the driving point admittance of the cell. Similar to real time analyses (Jonas et al. 1993; Rapp et al. 1994) this measurement characterizes the passive input impedance of the soma and dendritic cable. In addition, our frequency-domain approach characterizes the kinetic com-
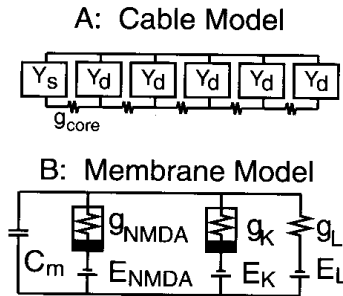
A: Cable Model

B: Membrane Model

Figure 1: The lumped soma-dendritic cable model of the whole cell (A) is composed of transverse admittances Y_s and Y_d for the cell membranes of the soma and dendritic compartments, respectively. The series of uniform dendritic compartments are linked by equal core conductances g_{core}. (B) The Hodgkin–Huxley type equivalent circuit for the cell membrane of each compartment.

ponents contributed by the active, voltage-dependent membrane conductances.

We have chosen to use a simple exponential functional relationship for the voltage dependence of the rate constants and have applied optimization techniques to the small-signal measurements made throughout an entire range of clamp potentials rather than at an individual voltage clamp step. Thus, the data obtained across a range of clamp potentials are used not only to optimize individual rate constants, but also to quantitatively determine their potential dependency.

The neuronal model is represented in the schematic (Fig. 1A) as an equivalent cable consisting of parallel elements for the cell membrane and transverse resistances representing the axial resistance to current flow through the neuroplasm. The membrane equivalent circuit (Fig. 1B) includes parallel elements representing the membrane capacitance and ionic conductances: (1) a passive leakage (g_L) conductance, (2) a slowly activated K conductance (g_K), and (3) an NMDA-sensitive (g_{NMDA}) conductance. Boxed resistors in the figure indicate time-variant, nonlinearly voltage-dependent conductances that arise from the nonlinear voltage-dependent kinetics of ion channel activation. Since the admittances, like conductances, add in parallel in the cell membrane, analysis of admittance permits graphic or algebraic separation of the total admittance into component parts. At the low frequency extreme this reduction of ad-

mittance into its component parts is analogous to the study of net and component membrane conductances under the steady-state conditions of a voltage-clamp step because the steady-state conductance is the value of the membrane admittance at zero frequency.

In this model NMDA activates a time-variant, voltage-dependent uniformly distributed conductance (Fig. 1B). The net driving-point admittance measured from the cell soma is a function of both the passive electrotonic properties of the cell and the time-variant, voltage-dependent active conductances distributed throughout (Ali-Hassan *et al.* 1992). The parameter estimation method was used to obtain quantitative estimates of the voltage-dependent ionic channel activation kinetics as well as the spatial distribution of channels located both on the soma and highly branched dendritic membranes.

The voltage-dependent parameters were estimated under soma voltage clamp conditions using cable models that explicitly incorporated the consequences of variations in effective electrotonic length with depolarization depending on the degree of channel activation. The experimentally determined membrane parameters were incorporated into nonlinear differential equations describing the properties of a single neuron with its dendritic structure.

2 Methods

Measurements were made on adult silver lampreys (*Ichthyomyzon unicuspis*) from 25 to 35 cm in length. A spinal cord–notochord preparation (Rovainen 1974; Rovainen 1979) as previously described (Moore and Buchanan 1993) was used. NMDA was bath applied at 0.1 mM in normal lamprey Ringer's solution (Moore and Buchanan 1993). The intracellular microelectrodes were filled with 4 M potassium acetate having resistances of 50–70 MΩ.

A combination voltage-clamp-frequency-domain method that we have previously described (Moore *et al.* 1993) was used for all experiments. In this method the cell soma is voltage clamped and the membrane current is measured in response to a small-signal stimulus composed of a sum of sinusoids superimposed on the clamp potential. The use of a voltage clamp rather than current clamp is important in these measurements because of the instability of neurons in the presence of NMDA. The ratio of the measured current to the stimulus voltage is the net driving-point admittance (inverse of impedance) of the parallel contribution of the cell soma and the dendritic tree. The admittance spectrum (Mauro *et al.* 1970) was obtained by taking the ratio of the fast Fourier transform (FFT) of the measured membrane current over the FFT of the voltage clamp stimulus of 2–3 mV root mean square dynamic amplitude (Moore *et al.* 1993). The Fourier synthesized stimulus has several advantages (Fishman 1992) including (1) low stimulus amplitude, (2) measurement at many frequen-

cies simultaneously during a single period of the stimulus, and (3) relative ease in achieving synchronization.

The stimulus signal used here was constructed from a frequency domain specification having a uniform stimulus amplitude spectrum and randomized phase spectrum over a range from 0.5 to 200 Hz. The constant magnitude spectrum drives the system uniformly at all frequencies of interest and a random phase spectrum was chosen to minimize the peak-to-peak dynamic amplitude of the stimulus waveform. A nonlinear least-squares parameter estimation method (Dennis et al. 1981) was used to determine model parameters for a 500 compartment dendritic cable that best fit the measured admittance spectrum. Depending on the length constant obtained from these cells the number of compartments can be greatly reduced for simulations of dynamic temporal response to low frequency stimuli.

The spatial step size of the dendritic compartments and thus the number of compartments was chosen to ensure accuracy of the parameter estimates. The step size was determined by increasing the number of compartments until variations in parameter estimates converged to within 0.1%. These parameters (Appendix B) were in turn used to predict the model's dynamic response to current clamp protocols. A variable step size, variable order backward differentiation integration method (Byrne and Hindmarsh 1975) was used to solve for the dynamic response. This electrically equivalent cable is an empirical model of the multicompartmental dendritic structure of the cell. Jonas et al. (1993) and Rapp et al. (1994) have made detailed analysis of passive models of pyramidal cells using time domain methods of estimating total membrane resistance and capacitance. The small-signal frequency-domain analysis presented here differs from these methods in its ability to explicitly fit parameters associated with the time- and voltage-dependent membrane ionic conductances. Although the results presented here consider only uniform, sequential compartments, the frequency-domain approach could be used with histologically determined multicompartmental models if receptor distributions could be assumed, or better still experimentally determined.

2.1 Membrane Model and Input Admittance.

Our membrane model for an individual compartment is composed of four parts: the membrane capacitance, a passive leakage (g_L) conductance, an NMDA-sensitive (g_{NMDA}) conductance (Appendix A), and a slowly activating potassium conductance (g_K) with kinetics on a time scale similar to that of the calcium-activated potassium conductance (Koch and Segev 1989). The total membrane current for an individual compartment in our model is the sum of the capacitive displacement current and the individual ionic currents.

$$I = C_m \frac{dV}{dt} + g_L(V - V_L) + g_K\,n(V - V_K) + g_{NMDA}\,m(V - V_{NMDA}) \qquad (2.1)$$

The NMDA and potassium conductance are gated by activation variables m and n, respectively, and driven by reversal potentials V_{NMDA} and V_K, respectively.

The total membrane admittance of an individual compartment is in turn defined in terms of the conductances and rate constants as previously described (Mauro et al. 1970; Moore and Buchanan 1993).

$$Y(s) = \frac{\delta I(s)}{\delta V(s)} \tag{2.2}$$

$$= sC + g_L$$

$$+ g_K \left\{ m_\infty + (V - V_{NMDA})\tau_m \frac{(\partial\alpha_m/\partial V) - m_\infty[(\partial\alpha_m/\partial V) + (\partial\beta_m/\partial V)]}{s\tau_m + 1} \right\}$$

$$+ g_{NMDA} \left\{ n_\infty + (V - V_K)\tau_n \frac{(\partial\alpha_n/\partial V) - n_\infty[(\partial\alpha_n/\partial V) + (\partial\beta_n/\partial V)]}{s\tau_n + 1} \right\}$$

The electrical equivalent for the lumped soma-dendritic cable circuit is shown in Figure 1A. The input admittance, Y_0, of the six compartment model as seen at the soma can be derived by reducing the network to an equivalent driving point admittance. If we number the soma compartment 0 and the most distal dendritic compartment 5 then we can derive the input admittance by beginning at the distal end of the cable and working toward the soma.

$$Y_5 = Y_d \tag{2.3}$$

$$Y_N = Y_d + \frac{Y_{N+1} g_{core}}{Y_{N+1} + g_{core}}, \qquad 1 \leq N \leq 4 \tag{2.4}$$

$$Y_0 = Y_s + \frac{Y_1 g_{core}}{Y_1 + g_{core}} \tag{2.5}$$

2.2 Kinetic Formulation. The dynamic behavior of Hodgkin–Huxley type ionic currents is in part determined by rate equations describing ion channel gating. In this formulation the usual kinetic variables are redefined in terms of the standard rate constants α and β. Each time-variant, voltage-dependent conductance in the model is gated by a single activation variable (e.g., m) that is described by a first order differential equation (equation 2.6) in which α_m and β_m are the opening and closing rate constants, respectively.

$$\frac{dm}{dt} = \alpha_m(1 - m) - \beta_m m \tag{2.6}$$

A common approach to characterizing the voltage dependence of gating

kinetics is to express them in terms of their steady-state value, m_∞, and time constant, τ_m.

$$\frac{dm}{dt} = (m_\infty - m)/\tau_m \tag{2.7}$$

$$m_\infty = \frac{\alpha_m}{\alpha_m + \beta_m} \tag{2.8}$$

$$\tau_m = 1/(\alpha_m + \beta_m) \tag{2.9}$$

We have chosen a specific formulation for the voltage dependent rate constants α and β (equations 2.10 and 2.11), which are parameterized by the magnitude and slope of the steady-state and time constant curves at half-activation as follows:

v_m is the half-activation ($m_\infty = 1/2$) voltage;

s_m is the slope of m_∞ at half-activation;

t_m is the time constant (τ_m) at half-activation; and

r_m is the normalized slope of τ_m at half-activation.

The four parameters chosen are orthogonal in their influence on the slope and magnitude of the steady-state and time constant curves. Using this formulation one can directly manipulate the steady-state or time constant curves and the magnitude independently of each curve's shape. This in turn enables one to constrain parameter estimates based on limits of the shapes and magnitudes of these curves, which has been of significant practical value in this study.

The dependence of the shape and magnitude of the steady-state m_∞ and time constant τ_m curves on each of the parameters is shown in Figure 2. Each row of plots shows variations in one of the four parameters. Variations in steady-state m_∞ curves are shown on the left and time constant τ_m curves are shown on the right.

$$\alpha_m = \frac{1}{2t_m} e^{(V-v_m)(2s_m-r_m)} \tag{2.10}$$

$$\beta_m = \frac{1}{2t_m} e^{-(V-v_m)(2s_m+r_m)} \tag{2.11}$$

$$m_\infty = \frac{1}{1 + e^{-4s_m(V-v_m)}} \tag{2.12}$$

$$\tau_m = \frac{2t_m}{e^{(V-v_m)(2s_m-r_m)} + e^{-(V-v_m)(2s_m+r_m)}} \tag{2.13}$$

The half-activation voltage v_m is defined as the membrane potential at which half the channels are open ($m_\infty = 1/2$) at steady state. Hyperpolarizing the half-activation voltage v_m from 0 to −50 mV shifts both the m_∞ and τ_m curves to the left without affecting the height or shape of the
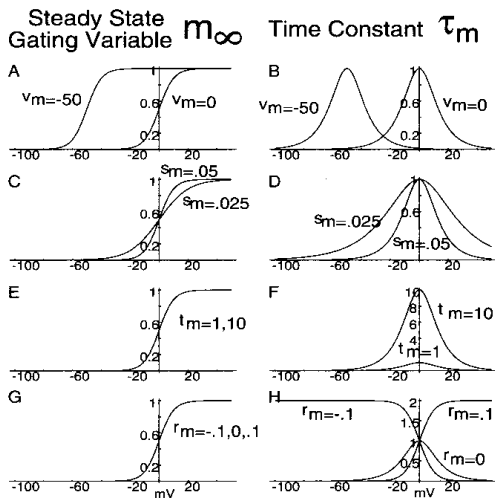
Figure 2: The influences of variations in the half-activation voltage v_m (A and B), the activation slope s_m (C, D), the half-activation time constant t_m (E, F), and the normalized time constant slope r_m (G, H) on the steady-state gating variable m_∞ (A, C, E, G) and the time constant τ_m (B, D, F, H). For each curve, unless stated otherwise, the parameter values are $v_m = 0$ mV, $s_m = 0.05$ mV^{-1}, $t_m = 1$ msec, and $r_m = 0$ mV^{-1}.

curves (Fig. 2A and B). Reducing the half-activation slope s_m from 0.05 to 0.025 mV^{-1} broadens the voltage dependence of both m_∞ and τ_m without affecting their magnitude or their center along the voltage axis (Fig. 2C and D). Increasing the half-activation time constant t_m from 1 to 10 msec increases the magnitude of τ_m without any shift along the voltage axis or any effect on the steady-state gating variable m_∞ (Fig. 2E and F). The time constant τ_m is symmetrical about the half-activation voltage v_m at $r_m = 0$. Changing the time constant slope r_m to 0.1 or -0.1 mV^{-1} skews the time constant curve toward voltages below or above v_m, respectively, without affecting the value of τ_m at $V = v_m$ and without affecting the steady-state gating variable m_∞ (Fig. 2G and H). The slope r_m is normalized with respect to the half-activation time constant t_m so that the shape of the time constant curve can be specified independently of the

magnitude scale. Since the steady-state curve is already normalized, the steady-state slope s_m does not require normalization. Thus, if experimental data consisting of time constants and steady-state values as a function of voltage are given, the four parameters v_m, s_m, t_m, and r_m can be varied to obtain initial estimates of the rate parameters. We have developed interactive software to efficiently achieve this on a Unix-based system.

It is of interest to consider that the value of t_m that alters the magnitude of τ_m has no effect on the steady-state curve. Similarly, the value of the slope, r_m, determines whether τ_m increases or decreases with voltage and is independent of the steady-state curve. For a value of $r_m = 0$ the curve is symmetrical above and below the half-activation voltage v_m. Values of r_m above and below 0 skew the curve toward increases or decreases of τ_m with membrane depolarization, respectively. The three conditions represented by $r_m = -0.1$, $+0.1$, and 0 cover markedly different data sets, notably kinetic processes whose rate increases, decreases, or does both over a range of potentials from resting or hyperpolarized values to increasing depolarizations. Although this analysis is largely empirical, it may be possible with molecular biological methods to obtain physical mechanisms for these opposite kinetic behaviors. The other two parameters, v_m and s_m, alter both m_∞ and τ_m.

Our formulation for α and β is equivalent to the following commonly used exponential form (Ascher and Nowak 1988).

$$\alpha_m = a e^{V/b} \tag{2.14}$$

$$\beta_m = c e^{-V/d} \tag{2.15}$$

The conversion from this parameter set to the modified formulation is shown below.

$$v_m = \frac{b\, d\, \log(c/a)}{b + d} \tag{2.16}$$

$$s_m = \frac{1}{4\,b} + \frac{1}{4\,d} \tag{2.17}$$

$$t_m = \left[a \left(\frac{c}{a} \right)^{d/d+b} + c \left(\frac{a}{c} \right)^{b/b+d} \right]^{-1} \tag{2.18}$$

$$r_m = \frac{-1}{2\,b} + \frac{1}{2\,d} \tag{2.19}$$

These kinetics can also be formulated in terms of the physical parameters that describe channels with bistable gating particles (Borg-Graham 1991). In the Borg-Graham notation α and β are defined in terms of a half-activation voltage $V_{1/2}$, a rate constant c_0, an *electrical distance* of the transition state from the outer edge of the membrane γ (Hille 1975), and an effective *particle valence* z:

$$\alpha = c_0 e^{\frac{-z\gamma(V - V_{1/2})F}{RT}} \tag{2.20}$$

$$\beta = c_0 e^{\frac{z(1-\gamma)(V - V_{1/2})F}{RT}} \tag{2.21}$$

where $V_{1/2} = v_m$ is the half-activation voltage as before, $t_m = 1/(2c_0)$, $r_m = (-1/2 + \gamma)zF/RT$, and $s_m = -zF/4RT$. Although the influences of $V_{1/2}$ and c_0 are orthogonal as before, the dependence of the shape of m_∞ and τ_m on the *particle valence* z and the *electrical distance* γ are not.

3 Results

It has been proposed (Brodin *et al.* 1991) that the shape of the TTX-resistant membrane potential oscillations (Sigvardt *et al.* 1985; Wallén and Grillner 1987) in lamprey spinal motorneurons is determined by the dynamic interaction of active inward and outward membrane ionic currents, however, the influences of passive properties and electrotonic current flow are less certain (Moore and Buchanan 1993). Traditional step voltage clamp methods in general require spatial homogeneity at the clamped voltage and thus prevent analysis of electrotonic current flow in nonhomogeneous structures such as a soma coupled to a dendritic tree (Rall 1959; Rall 1969).

In the frequency domain the Hodgkin–Huxley type formulation of a time-varying active membrane ionic conductance yields a frequency-dependent response (Mauro *et al.* 1970) to sinusoidal voltage clamp stimuli (Fishman 1992; Koch 1984). Figure 3 illustrates a part of a data set fitted over a range of membrane potentials from -92 to -47 mV. In this potential range the magnitude of the impedance at low frequencies is initially enhanced by NMDA activation and at the more depolarized potentials is decreased. This behavior occurs because the algebraic addition of admittances and slope conductances is such that the individual positive and negative conductance can cancel each other to cause a net decrease, and thus a resistance increase. In Figure 3 the reversal of this effect is observed at -57 mV where the impedance magnitude with NMDA is decreased at $V = -72$ mV compared to -82 mV. A pronounced phase change indicative of a net negative conductance is clearly demonstrated at all the potentials shown in Figure 3. All of the NMDA-induced effects are abolished at potentials more negative than -90 mV. As the NMDA-induced negative conductance increases with depolarization, it first acts to counterbalance positive conductances until a null point is reached at which the net positive and negative conductances are nearly equal. This is shown at -82 mV with NMDA where at low frequencies the admittance locus approaches the origin in the complex plane (Fig. 3C) and the corresponding impedance magnitude function reaches a maximal value at 0.5 Hz (Fig. 3A). With further depolarization the negative conductance continues to increase until the system becomes potentially unstable under current clamp conditions because the total conductance has a net negative value. However, this can be measured under voltage clamp conditions and is indicated by phase functions more negative than $\pi/2$ radians ($-90°$). At the most depolarized potentials the phase function
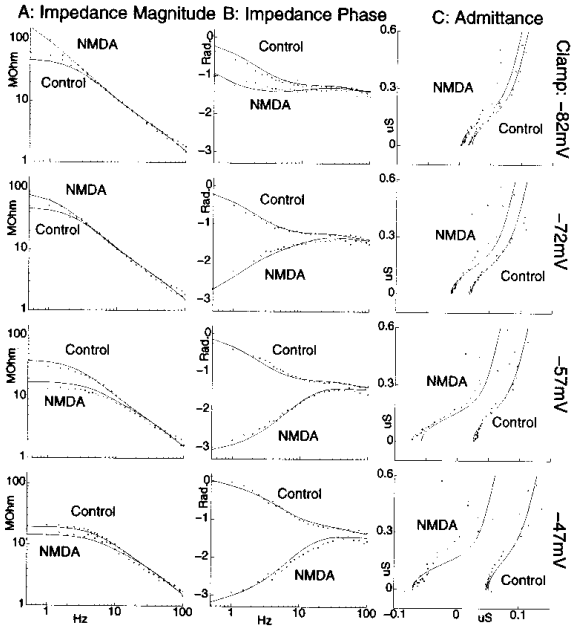
Figure 3: The voltage and NMDA dependence of the somatic input impedance magnitude and phase are shown in columns A and B, respectively. Measurements (symbols) and model-generated fits (solid lines) are shown at four clamp potentials, −82, −72, −57, and −47 mV. Column C shows the real versus the imaginary parts of the admittance (algebraic inverse of impedance) in the complex plane with real and imaginary axes plotted horizontally and vertically, respectively. Fixed values for the NMDA kinetics and reversal potentials were assumed at $v_m = -19.9$ mV, $s_m = 0.02$ mV^{-1}, $t_m = 0.00014$ sec, $r_m = 0.0187$ mV^{-1}, $V_K = -85$ mV, $V_{NMDA} = 0$ mV, and the number of compartments was fixed at 500. The remaining best-fit parameter estimates were $C_m = 0.845$ nF, $g_K = 0.0239$ μS for control and 0.0296 μS for NMDA, $g_L = 0.0112$ μS, $g_{NMDA} = 0.242$ μS, $L = 0.505$, $a = 0.933$, $v_n = -47.9$ mV, $s_n = 0.167$ mV^{-1}, $t_n = 9.97$ sec, and $r_n = -0.05$ mV^{-1}. See text for parameter definitions.

shows a systematic voltage-dependent shift with respect to the control values even at the high frequencies. The high frequency effects are more dramatically illustrated by plots of the real versus imaginary parts of the admittance shown in Figure 3 where the uppermost points in column C represent high frequencies. These plots clearly show that there is a voltage-dependent shift at all frequencies of the admittance that is reasonably well approximated by a neuronal model with NMDA receptors uniformly distributed over the entire dendritic tree. The shift in the admittance plots at high frequencies was observed in five analyzed lamprey neurons.

Figure 4 is a comparison of the admittance of several neuronal structures and receptor distributions to better illustrate an interpretation of admittance plots in the complex plane. Although the effects of dendritic cables are relatively easy to observe in frequency domain data plotted as magnitude and phase, their influence is even more dramatic in the admittance plots. A resistance alone would appear as a single point on the real (horizontal) axis. A passive isopotential compartment (simple RC circuit) with no dendritic cable in Figure 4A would plot as a straight line extending upward with increasing frequency from the dc conductance lying on the real axis. However, the addition of a cable to the soma shows an inflection between the low and high frequency portions of the curve. In general an increase in a positive membrane conductance that is uniformly distributed over the cable will shift the curve to the right, i.e., in the direction of an increased real part of the admittance. On the other hand the activation of a negative conductance will shift the curve to the left. Figure 4B illustrates that if there are only peripheral NMDA receptors in the model, then only the low frequency (bottom) portion of the curve shifts. By contrast if there are only central (somatic) NMDA receptors the curve shifts uniformly to the left with negligible change in shape.

Superimposed plots of the admittance functions are shown in Figure 5 illustrating a shift to the right for the control curves where only a positive conductance was activated and a pronounced shift to the left for activation of NMDA receptors. Despite the scatter in the data, the optimization method provided a clearly improved fit using a model with uniformly distributed conductances compared to one containing only peripheral receptors. An alternative complex impedance plane plot of this data is also given in Figure 5 illustrating that the activation of the negative conductance reaches a null point at near −77 mV. At more depolarized potentials the real part of the admittance is negative under these experimental conditions, where the potential at which a shift from positive to negative values occurs between −87 and −77 mV. In contrast, the control curves shift in the opposite direction with depolarization. To some extent the activation of the positive versus the negative conductances produces mirror images in the complex-plane impedance plots.

The results shown in Figures 3 and 5 were from a cell that did not show any indication of resonance behavior. Resonance in the impedance
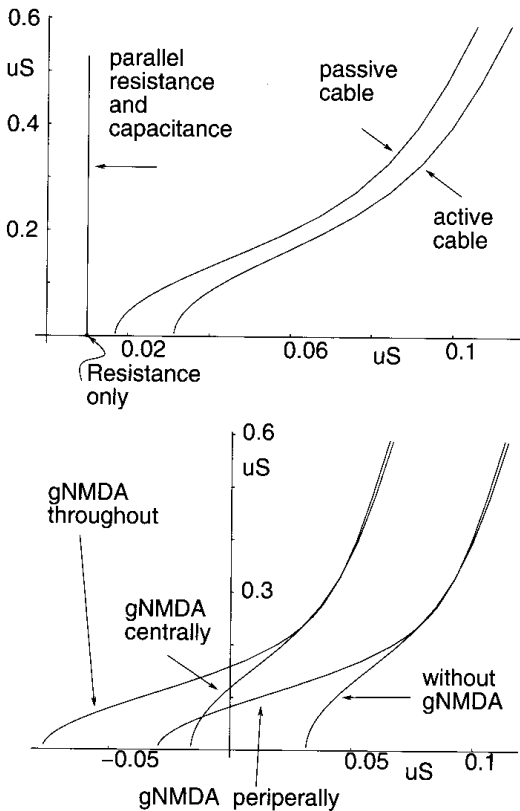
Figure 4: (A) The admittance of reduced models including (1) a passive leakage resistance, (2) a leakage resistance and capacitance in parallel, (3) a passive cable, and (4) an active cable containing a potassium conductance. (B) The admittance of the whole cell model for peripheral versus central variations in the spatial distribution of NMDA-activated conductance. See Figure 3 for parameter values.
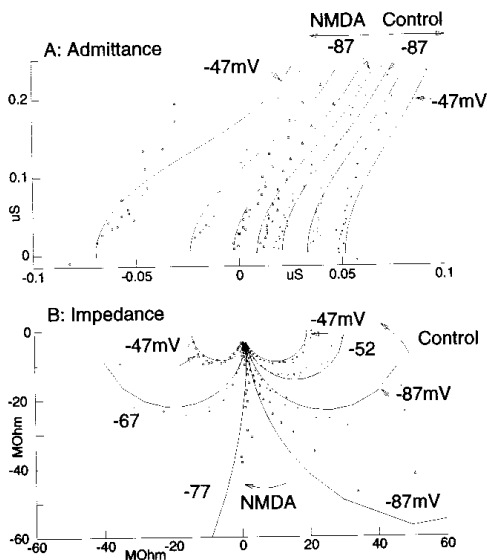
Figure 5: Experimentally measured (x) and model-generated (solid lines) input admittance is shown in A at clamp potentials of −87, −77, −67, and −47 mV in the presence of bath-applied NMDA and at −87, −52, and −47 mV without NMDA. The data are shown again as real versus imaginary parts of the input impedance in B. Measurements and parameter estimates here are taken from the same cell as in Figure 3.

magnitude is clearly observed in some neurons and also can occur with the model system. Figure 6 illustrates a neuron showing clear resonance behavior. The ability of a negative conductance system to show resonance is a consequence of a balance between the passive electrotonic structure and the relative values of the positive and negative conductance systems. Both the resonating and nonresonating neurons show oscillatory behavior under current clamp conditions and have regions of instability in their impedance functions. Figure 6 also illustrates that resonance manifests itself in the complex-plane admittance plot as an admittance function that passes through the origin at relatively low frequencies.
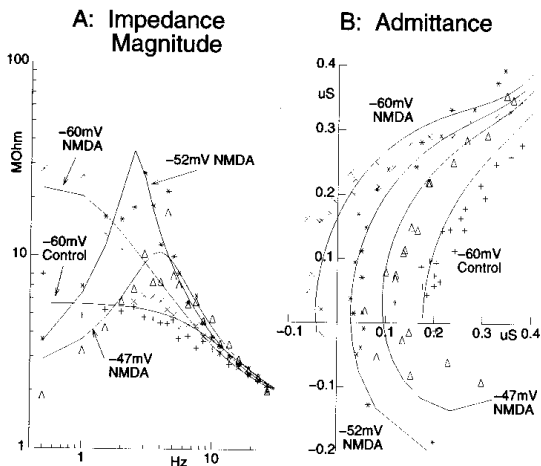
Figure 6: Measured (x) and model-fitted (solid lines) input impedance magnitude are shown in A at clamp potentials of −60, −52, and −47 mV in the presence of bath-applied NMDA and at −60 mV without NMDA. The data are shown again as real versus imaginary parts of the input admittance in B. The estimated parameter values were $C_m = 0.05$ nF, $g_L = 0.00236$ μS, $g_{NMDA} = 0.0218$ μS, $g_K = 0$, $g_{K,NMDA} = 0.0045$ μS, $L = 1.08$, $a = 101.5$, $v_n = -52.2$ mV, $s_n = 0.175$ mV^{-1}, $t_n = 1.08$ sec, and $r_n = -0.2$ mV^{-1}. The remaining parameter values are identical to those in Figure 3.

The final test of this analysis is the ability of the complete set of nonlinear equations to produce the constant current behavior observed in these neurons. Figure 7 shows the solution for a hyperpolarizing current of −0.634 nA of the whole cell model equations (Appendix A), which consist of a soma plus a series of five identical dendritic compartments forming a ladder network. As is typical of NMDA-sensitive neurons in the presence of 10 μM TTX, the model neuron shows pacemaker oscillations from 0.1–5 Hz (Morris and Lecar 1981; Wang and Rinzel 1993). The plateau potential is sustained by the NMDA-induced inward current, which is followed by a repolarizing outward current. The period of the oscillation is principally determined by the slower outward current
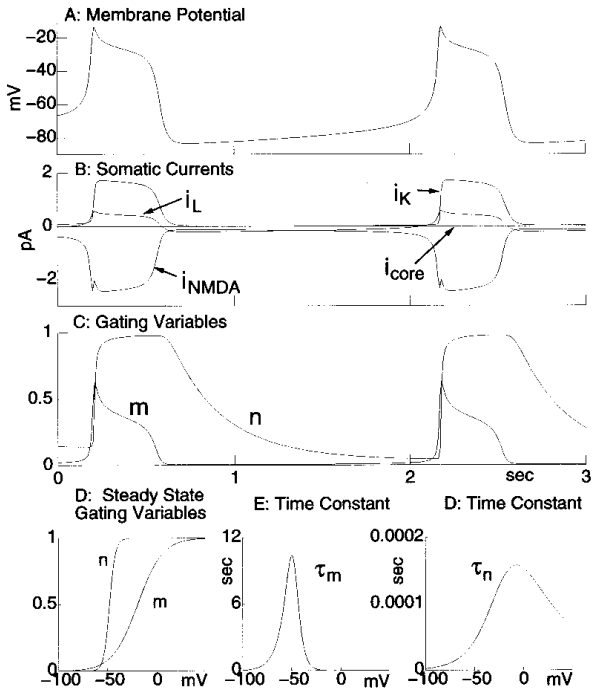
Figure 7: Model-generated current clamp response to a steady hyperpolarizing stimulus of -0.643 nA and application of NMDA. The membrane potential oscillation (A), somatic membrane currents (B), their gating variables (C), and their steady-state gating variables (D) are shown. The parameter values here are identical to those in Figure 3 where $N = 5$ and $V_L = -65$ mV.

whose gating variable also has a relatively steep voltage dependence. Such a steep voltage dependence is probably necessary to achieve rapid repolarization of the plateau potential.

4 Discussion

Neurons are nonlinear dynamic systems consisting of complex cable structures that are generally not accessible. Conventional voltage clamp methods requiring spatial and time control of the membrane potential cannot be rigorously applied to a determination of the biophysical properties of these branching structures. The quantitative analysis using frequency domain techniques presented here takes into account some of the difficulties with space clamp problems, however, there remain certain fundamental problems for dendrites possessing long electrotonic lengths. The number of compartments used in simulating the current clamp response was selected to ensure that the spatial resolution, or length of each compartment, was less than two-tenths of the passive space constant λ (Koch and Segev 1989). Furthermore, the presence of a negative conductance will enhance the dc space constant if stability conditions are met. Therefore, the experimental conditions used in the measurements presented generally allowed for relatively uniform dc membrane potentials and a compartmental size that was acceptable for computing nonlinear behavior (Koch and Segev 1989; Rall 1969). Dendritic structures that do not meet these criteria will require a consideration of the potential profile along the cable as well as a determination of the minimum number of compartments required for adequate spatial resolution.

The investigation of nonlinear neuronal systems by piecewise linear analysis is proposed in this paper as a method that can provide kinetic information needed to model complex neurons. It will be useful to implement other nonlinear analytical methods such as kernel analysis (Marmarelis and Marmarelis 1978; Victor *et al.* 1977) to compare different kinetic models and further verify the validity of the different approaches. It is remarkable that the analytical approach proposed by Hodgkin and Huxley over 40 years ago continues to be among the most pragmatic to obtain kinetic information for neuronal models. It is noteworthy that the HH analysis is not exactly a piecewise linearization since large signal voltage clamp steps are used, however, their analysis of the kinetic response was made with a hybrid system using a linear kinetic model that was incorporated in a power function to give a delay in the conductance response to a step voltage clamp. Thus, the principal nonlinearity due to the potential dependence of the rate constants was essentially linearized by the voltage clamp. As K. C. Cole stated, the voltage clamp tamed the axon (Cole 1968).

The use of piecewise linear analysis to obtain voltage-dependent rate constants for the simulation of a nonlinear kinetic system of equations is unusual in at least two respects: (1) as discussed above, this approach provides a verifiable description of the nonlinear system, and (2) if the system is unstable it still may be possible to obtain a steady-state small-signal response by applying the voltage clamp to control the membrane and prevent oscillations. This approach is questionable if the electrotonic

length of the dendritic cable is much larger than one. Although the analysis shown in Figure 6 gives a passive electrotonic length (L) of 1.08, in the presence of NMDA the effective electrotonic length at dc is either considerably less than one or undefined, depending on the magnitude of the negative conductance component. In the case where L is defined, the $< 0.2\lambda$ criteria are easily met. If the total membrane conductance is net negative then L would have an imaginary value using standard definitions of the space constant. This condition is clearly oscillatory, however, it does appear to be controlled by the point voltage clamp in the soma. We have not observed oscillations in the currents during a voltage clamp of the soma in these cells, which would not have been the case if the electrotonic length of the dendritic cable was much larger than one. Thus, the methodology used in these experiments relies on specific aspects of the neuronal system that must always be verified.

As a case in point, if a positive conductance were being activated in a neuron whose electrotonic length is well above one and increasing with depolarizations, then the potential profile along the cable must be considered. Our analysis of a positive conductance for the cell of Figure 3 gives values of an effective electrotonic length from 0.3 to 1.8 for a membrane potential range of -87 to -47 mV.

The choice of simple exponential functions for the voltage dependence of the rate constants was principally based on earlier descriptions of NMDA and voltage induced channel kinetics (Ascher and Nowak 1988; Borg-Graham 1991; Holmes and Levy 1990). There are many variants of combinations of exponential functions used for channel descriptions and it is not clear if any of these descriptions have a fundamental basis. It would be useful to rigorously analyze different channel kinetics of space clamped cells to quantitatively determine the best description for the voltage dependency of rate constants. Unfortunately, this has not been done and our view is that the simpler formalism is adequate until more quantitative analyses are done. As was shown above, the use of exponential functions allows the development of an efficient method to obtain initial estimates of kinetic parameters. This is an essential practical point if parameter optimization methods are to be successfully used.

Appendix A: Whole Cell Model Equations

All values in the following tables are in units of s, mV, nA, μS, MΩ, and nF unless otherwise specified. The real and imaginary parts of complex frequency, $s = \sigma + j2\pi f$, where f is in Hz.

$$i_L = g_L(V - V_L) \tag{A.1}$$

$$i_{NMDA} = g_{NMDA}\, m\,(V - V_{NMDA}) \tag{A.2}$$

$$i_K = g_K\, n\,(V - V_K) \tag{A.3}$$

$$i_{core} = g_{core}\,(V_i - V_{i+1}) \tag{A.4}$$

$$i_{\text{soma}} = i_K + i_{\text{core}} + i_L + i_{\text{NMDA}} \tag{A.5}$$

$$\frac{dV_{\text{soma}}}{dt} = \frac{i_{\text{soma}}}{C_{\text{soma}}} + g_{\text{core}}(V_{\text{soma}} - V_{\text{dend},1}) \tag{A.6}$$

$$i_{\text{dend},j} = \frac{a}{n}g_L(V_{\text{dend},j} - V_L) \tag{A.7}$$

$$+ \frac{a}{n}g_K\, n_j\,(V_{\text{dend},j} - V_K)$$

$$+ \frac{a}{n}g_{\text{NMDA}}\, m_j\,(V_{\text{dend},j} - V_{\text{NMDA}})$$

$$\frac{dV_{\text{dend},j}}{dt} = \frac{-N}{aC_{\text{soma}}}[i_{\text{dend},j} + g_{\text{core}}(V_{\text{dend},j} - V_{\text{dend},j-1}) \tag{A.8}$$

$$+ g_{\text{core}}(V_{\text{dend},j} - V_{\text{dend},j+1})], \qquad j = 1\ldots N-1$$

$$\frac{dV_{\text{dend},N}}{dt} = \frac{-N}{aC_{\text{soma}}}[i_{\text{dend},N} + g_{\text{core}}(V_{\text{dend},N} - V_{\text{dend},N-1})] \tag{A.9}$$

Appendix B: Somatic Input Admittance Model

$$\frac{\delta\alpha_m}{\delta V} = \frac{(-r_m + 2s_m)}{2\,t_m}e^{(-r_m + 2s_m)\,(V - v_m)} \tag{B.1}$$

$$\frac{\delta\beta_m}{\delta V} = \frac{(-r_m - 2s_m)}{2\,t_m}e^{(-r_m - 2s_m)\,(V - v_m)} \tag{B.2}$$

$$Y_s = \frac{\delta I(s)}{\delta V(s)} \tag{B.3}$$

$$= sC + g_L \tag{B.4}$$

$$+ g_K\left\{ m_\infty + (V - V_{\text{NMDA}})\tau_m\frac{(\partial\alpha_m/\partial V) - m_\infty[(\partial\alpha_m/\partial V) + (\partial\beta_m/\partial V)]}{s\tau_m + 1}\right\}$$

$$+ g_{\text{NMDA}}\left\{ n_\infty + (V - V_K)\tau_n\frac{(\partial\alpha_n/\partial V) - n_\infty[(\partial\alpha_n/\partial V) + (\partial\beta_n/\partial V)]}{s\tau_n + 1}\right\}$$

$$Y_d = \frac{a}{N}Y_s \tag{B.5}$$

$$Y_N = Y_d \tag{B.6}$$

$$Y_n = Y_d + \frac{Y_{n+1}\,g_{\text{core}}}{Y_{n+1} + g_{\text{core}}}, \qquad n = 1\ldots N-1 \tag{B.7}$$

$$Y_0 = Y_s + \frac{Y_1\,g_{\text{core}}}{Y_1 + g_{\text{core}}} \tag{B.8}$$

Acknowledgments

References

Ali-Hassan, W., Saidel, G., and Durand, D. 1992. Estimation of electrotonic parameters using an inverse Fourier transform technique. *IEEE Trans. Biomed. Eng.* **39**, 493–501.

Ascher, P., and Nowak, L. 1988. The role of divalent cations in the n-methyl-d-aspartate responses of mouse central neurones in culture. *J. Physiol.* **399**, 247–266.

Borg-Graham, L. 1991. Modelling the non-linear conductances of excitable membranes. In *Cellular Neurobiology: A Practical Approach*, J. Chad and H. Wheal, eds., ch. 13, pp. 247–275. Oxford University Press, New York.

Brodin, L., Tråvén, G., Lansner, A., Wallén, P., Ekeberg, Ö., and Grillner, S. 1991. Computer simulations of n-methyl-d-aspartate receptor-induced membrane properties in a neuron model. *J. Neurophysiol.* **66**, 473–484.

Byrne, G., and Hindmarsh, A. 1975. A polyalgorithm for the numerical solution of ordinary differential equations. *ACM Trans. Math. Software* **1**, 71–96.

Cole, K. 1968. *Membranes, Ions and Impulses*. University of California Press, Berkeley.

Dennis, J., Gay, D., and Welsch, R. 1981. An adaptive nonlinear least-squares algorithm. *ACM Trans. Math. Software* **7**(3).

Fishman, H. 1992. Assessment of conduction properties and thermal noise in cell membranes by admittance spectroscopy. *Bioelectromagnet. Suppl.* **1**, 78–100.

Hille, B. 1975. Ion selectivity of Na and K channels of nerve membranes. In *Membranes: Lipid Bilayers and Biological Membranes: Dynamic Properties*, G. Eisenman, ed., ch. 4, p. 281. Marcel Dekker, New York.

Hodgkin, A., and Huxley, A. 1952. A quantitative description of membrane current and its application to conduction and excitation in nerve. *J. Physiol.* **117**, 500–544.

Holmes, W., and Levy, W. 1990. Insights into associative long-term potentiation from computational models of NMDA receptor-mediated calcium influx and intracellular calcium concentration changes. *J. Neurophysiol.* **63**, 1148–1168.

Jonas, P., Major, G., and Sakmann, B. 1993. Quantal components of unitary EPSCs at the mossy fibre synapse on CA3 pyramidal cells of rat hippocampus. *J. Physiol.* **472**, 615–663.

Koch, C. 1984. Cable theory in neurons with active, linearized membranes. *Biol. Cyber.* **50**, 15–33.

Koch, E. C., and Segev, I. 1989. *Methods in Neuronal Modeling*. MIT Press, Cambridge.

Marmarelis, P., and Marmarelis, V. 1978. *Analysis of Physiological Systems. The White Noise Approach*. Plenum, New York.

Mauro, A., Conti, F., Dodge, F., and Schor, R. 1970. Subthreshold behavior and phenomenological impedance of the squid giant axon. *J. Gen. Physiol.* **55**, 497–523.

Moore, L., and Buchanan, J. 1993. The effects of neurotransmitters on the integrative properties of spinal neurons of the lamprey. *J. Exp. Biol.* **175**, 89–113.

Moore, L., Hill, R., and Grillner, S. 1993. Voltage clamp frequency domain analysis of NMDA activated neurons. *J. Exp. Biol.* **175**, 59–87.

Morris, C., and Lecar, H. 1981. Voltage oscillations in the barnacle giant muscle fiber. *Biophys. J.* **35**, 193–213.

Rall, W. 1959. Branching dendritic trees and motorneuron membrane resistivity. *Exp. Neurol.* **1**, 491–527.

Rall, W. 1969. Time constants and electrotonic length of membrane cylinders and neurons. *Biophys. J.* **9**, 1483–1508.

Rapp, M., Segev, I., and Yarom, Y. 1994. Physiology, morphology and detailed passive models of guinea-pig cerebellar Purkinje cells. *J. Physiol.* **474**, 101–118.

Rovainen, C. 1974. Synaptic interactions of identified nerve cells in the spinal cord of the sea lamprey. *J. Comp. Neurol.* **154**, 189–206.

Rovainen, C. 1979. Neurobiology of lampreys. *Physiol. Rev.* **59**, 1007–1077.

Sigvardt, K., Grillner, S., Wallén, P., and van Dongen, P. 1985. Activation of NMDA receptor elicits fictive locomotion and bistable membrane properties in the lamprey spinal cord. *Brain Res.* **336**, 390–395.

Victor, J., Shapley, R., and Knight, B. 1977. Non-linear analysis of retinal ganglion cells in the frequency domain. *Proc. Natl. Acad. Sci. U.S.A.* **74**, 3068–3072.

Wallén, P., and Grillner, S. 1987. N-methyl-d-aspartate receptor-induced, inherent oscillatory activity in neurons active during fictive locomotion in the lamprey. *J. Neurosci.* **7**, 2745–2755.

Wang, X., and Rinzel, J. 1993. Spindle rhythmicity in the reticularis thalami nucleus: Synchronization among mutually inhibitory neurons. *Neuroscience* **53**(4), 899–904.